Ultrafast electron dynamics in the charge density wave material TbTe$_3$

New Journal of Physics

Ultrafast electron dynamics in the charge density wave material TbTe$_3$

F Schmitt[1,5]**, P S Kirchmann**[1,2]**, U Bovensiepen**[2,3,7]**,
R G Moore**[4,5]**, J-H Chu**[5]**, D H Lu**[4]**, L Rettig**[2]**, M Wolf**[2,6]**,
I R Fisher**[1,5] **and Z-X Shen**[1,4,5,7]

[1] Stanford Institute for Materials and Energy Science, SLAC National Accelerator Laboratory, 2575 Sand Hill Road, Menlo Park, CA 94025, USA
[2] Fachbereich Physik, Freie Universität Berlin, Arnimallee 14, 14195 Berlin, Germany
[3] Fakultät für Physik, Universität Duisburg-Essen, Lotharstrasse 1, 47048 Duisburg, Germany
[4] Stanford Synchrotron Radiation Laboratory, 2575 Sand Hill Road, Menlo Park, CA 94025, USA
[5] Geballe Laboratory for Advanced Materials, Departments of Physics and Applied Physics, Stanford University, 476 Lomita Mall, Stanford, CA 94305, USA
[6] Department of Physical Chemistry, Fritz Haber Institute of the Max Planck Society, Faradayweg 4-6, 14195 Berlin, Germany
E-mail: zxshen@stanford.edu and uwe.bovensiepen@uni-due.de

Abstract. Gaining insights into the mechanisms of how order and broken symmetry emerges from many-particle interactions is a major challenge in solid state physics. Most experimental techniques—such as angle-resolved photoemission spectroscopy (ARPES)—probe the single-particle excitation spectrum and extract information about the ordering mechanism and collective effects, often indirectly through theory. Time-resolved ARPES (tr-ARPES) makes collective dynamics of a system after optical excitation directly visible through their influence on the quasi-particle band structure. Using this technique, we present a systematic study of TbTe$_3$, a metal that exhibits a charge-density wave (CDW) transition. We discuss time-resolved data taken at different positions in the Brillouin zone (BZ) and at different temperatures.

[7] Authors to whom any correspondence should be addressed.

The transient change in the band structure due to the excitation is qualitatively different between the region gapped by the CDW order vector and an ungapped but otherwise equivalent region. Also, we discovered two distinct collective modes at roughly 3.5 and 2.5 THz, the latter of which only occurs in the CDW band near the gapped region, demonstrating the strength of tr-ARPES in discerning the origin of the modes from the way in which they couple to the quasi-particle bands. In addition, a systematic pump fluence dependence in the gapped region documents the crossover from a weakly perturbed to a strongly perturbed regime, which can be related to a crossover from a regime where mainly the amplitude mode gets excited to a regime where the CDW gap closes at least partially.

Contents

1. Introduction

Competition between order and fluctuations is central to the field of solid state physics. While the interaction between pairs of (quasi-)particles can sometimes be cast into simple terms and pictures, the inclusion of many particles and the competition between two or more interactions and/or fluctuations lead to the emergence of rich and complex kinds of broken symmetry states in solids. One of the competing forces can be thermal fluctuations, but quantum fluctuations are also possible in the case of a quantum critical point at $T = 0$ [1]. The possible interactions leading to order are numerous. For example, coulomb repulsion between electrons is responsible for Mott physics [2–4], as observed in e.g. the high-temperature superconducting cuprates [5]. The interaction of electron spins can lead to spin density waves and antiferromagnetism, and it causes a wide variety of states of matter in heavy fermion systems due to the competition between the Kondo and Ruderman–Kittel–Kasuya–Yosida (RKKY) interactions [6–9]. The interaction between electrons and the lattice is the basis for conventional superconductivity [10, 11] and charge density waves [6], just to name a few. Hence, an understanding of the microscopic mechanisms that couple these quasi-particle excitations and the manner in which they lead to ordered ground states is vital for understanding many-body effects in solids in general [1, 2, 4].

It is not trivial to separate the contributions of individual degrees of freedom from the ordering mechanism in thermodynamic equilibrium. One approach is to use angle-resolved photoelectron spectroscopy (ARPES) to study the renormalization of quasi-particle band

dispersions due to the interaction with bosonic modes, such as phonons and magnons [5]. In ARPES, ultraviolet (UV) light excites bound quasi-particle states via multipole matrix elements, which are then projected into free-electron vacuum states. Therefore, ARPES is a powerful tool for obtaining the single-particle spectral function $A(\vec{k}_{\parallel}, \omega)$ as a function of electron momentum $\vec{k}_{\parallel}$ and energy ω [12]. Depending on the details of the bosonic coupling, this dispersion renormalization can be detected as abrupt changes of the slope, the so-called kinks in the electronic dispersion relation [5, 13]. A careful analysis of this dispersion renormalization allows one to establish an energy scale for the involved boson modes, and provides information about the momentum dependence of the electron–boson coupling. The renormalization of the spectral function can be expressed [5] in terms of an electronic self-energy $\Sigma(\vec{k}, \omega)$,

$$A(\vec{k}, \omega) = -\frac{1}{\pi} \frac{\Sigma''(\vec{k}, \omega)}{[\omega - \epsilon(\vec{k}) - \Sigma'(\vec{k}, \omega)]^2 + [\Sigma''(\vec{k}, \omega)]^2}. \tag{1}$$

Here, $\Sigma' = \mathrm{Re}(\Sigma)$ and $\Sigma'' = \mathrm{Im}(\Sigma)$ are the real and imaginary parts of the electronic self-energy. For a given bare band dispersion $\epsilon(\vec{k})$, $\mathrm{Re}(\Sigma)$ can be extracted from the ARPES spectra by subtracting $\epsilon(\vec{k})$ from the band position extracted from the data, while $\mathrm{Im}(\Sigma)$ corresponds to the line width (or inverse quasi-particle lifetime) of the ARPES data [5].

However, a precise knowledge of the bare, unrenormalized band is required but not always available. Furthermore, it is not necessarily easy to determine what causes the renormalization. Often enough, there exist many different kinds of interactions simultaneously in correlated materials, all of which can contribute to the renormalization to various degrees, making it hard to distinguish between them. In recent years, the complementary approach of time-resolved ARPES (tr-ARPES) has been developed [14–16]. In tr-ARPES, an intense ultrashort femtosecond (1 fs = 10^{-15} s) pump laser pulse first excites the electronic system and the effect on the spectral function is probed by ARPES with a time-delayed femtosecond UV probe laser pulse. This approach allows one to obtain the spectral function $A(\vec{k}, \omega, t)$ as a function of *both* electron energy ω and pump–probe time delay t.

In combining information from the frequency and time domains, tr-ARPES provides access to both single-particle properties and collective many-body phenomena at once. By observing the time-dependent changes in the transient spectral function $A(t)$, correlations and many particle excitations become visible via their influence on the quasi-particles. In favorable cases, a dominant single mode of frequency Ω is detected by a periodic modification of $A(t)$. For this to be observable, a mode has to be excited with phase coherence with respect to an impulsive excitation: this can be achieved in several ways [17], but with the exception of infrared (IR) resonant vibrational excitations where a Fourier component of the pump pulse is in resonance with a vibration, the duration of the optical excitation is required to be shorter than half the oscillation period $T/2 = \pi/\Omega$ [17]. Since typical collective excitations, such as optical phonons or spin waves, have energies $\hbar\Omega$ of about 10–100 meV, their period $T = 2\pi/\Omega$ is well in the femtosecond regime. Furthermore, electron and hole lifetimes can be detected; the decay of electronic excitations in metals occurs on timescales of several fs to a few hundreds of fs [18].

Hence, an experimental tool that probes these collective excitations in real time would require femtosecond time-resolution. This can be achieved by the use of Ti:sapphire lasers, which emit femtosecond laser pulses centered near 800 nm wavelength (i.e. photon energies of $h\nu \approx 1.5$ eV) by mode locking of the broadband Ti:sapphire emission. Photoemission studies require femtosecond laser pulses in the UV spectral range that are generated by 800 nm laser pulses in nonlinear optical crystals up to the fourth harmonic [19, 20], or in rare gases to even
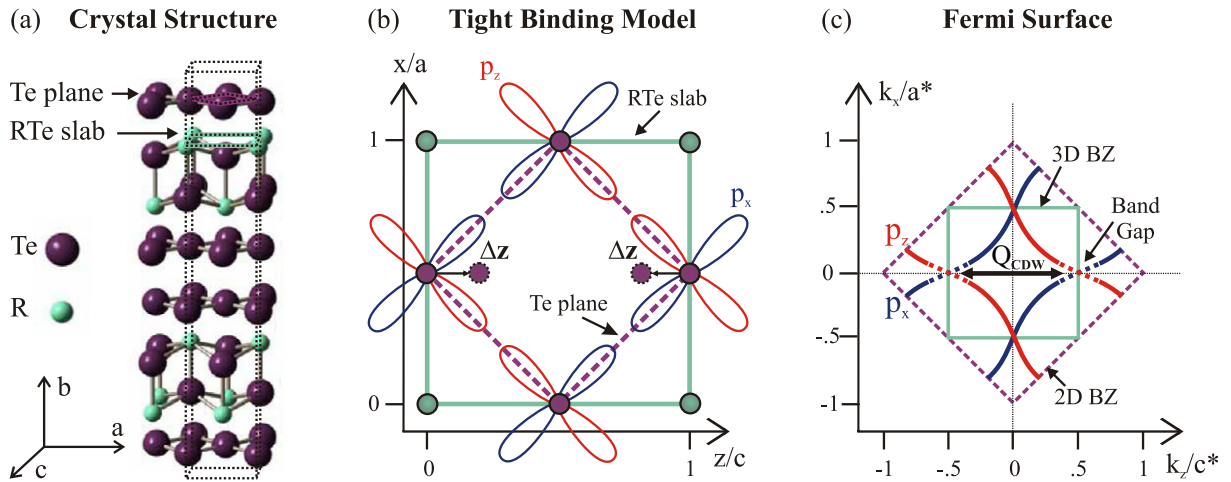
Figure 1. (a) The crystal structure of RTe$_3$ [25] is composed of square Te planes and buckled RTe slabs (R = lanthanide). Note that the b-axis in the space group Cmcm of RTe$_3$ is perpendicular to the Te plane with $b = 25.7$ Å $\gg a \approx c = 4.3 \ldots 4.5$ Å [26]. The crystals cleave between two RTe slabs. (b) Real-space model of the square-planar Te sheet with 2D (solid purple line) and 3D (dashed green line) unit cells of the Te planes and the RTe slab, respectively. The Te p_x (red) and p_z (blue) orbitals as well as the lattice distortion Δz due to the CDW are depicted. (c) FS calculated in the tight-binding model. The extended 2D (dashed) and reduced 3D BZ (solid) are indicated. The small perpendicular coupling between the p_x and p_z orbitals results in two sets of quasi-1D bands and an almost square FS. The nesting of the phonon mode with nesting vector Q_{CDW} opens two bandgaps along the z-direction [27].

higher harmonics [21, 22]. Optical excitation by the fundamental IR laser pulse at $h\nu \approx 1.5$ eV and subsequent probing of the dynamics of bound electrons via photoemission by the UV laser pulse at $4 \cdot h\nu \approx 6.0$ eV will allow us to monitor the periodic binding energy variations of localized electronic states: a coherently excited phonon modulates internuclear distances in the lattice, leading to modulations in the electronic band structure [14, 23]. Angular-dependent studies of high-temperature superconductors [24] and CDW materials [16] establish tr-ARPES as a powerful tool for the investigation of collective excitation modes in complex materials.

Here, we present a tr-ARPES investigation of the quasi-two-dimensional (quasi-2D) CDW model system TbTe$_3$ where we study the collective excitation modes after ultrafast optical laser excitation. In general, CDW materials are among the well-established model systems that have had a considerable impact on our understanding of quantum many-body problems [6]. In brief, a CDW is a broken symmetry ground state with spatially modulated electron and corresponding ion densities. It can form at low temperatures in low-dimensional materials with high densities of states at the Fermi level E_F due to a combination of an electron susceptibility that is strongly enhanced at E_F and strong, possibly anisotropic, electron–phonon coupling. The driving force of this coupled electron–lattice instability is the minimization of the system's total energy, which is achieved by the reduction of the kinetic electron energy due to an opening of a bandgap at the Fermi surface (FS). This is a consequence of a spontaneous periodic lattice modulation Δz (see figure 1(b)) with an appropriate wave vector Q_{CDW} (see figure 1(c)) that nests parts of the FS.

The coupled electron–lattice dynamics of CDW systems are characterized by well-defined collective excitation modes: phase and amplitude modes. In a phase mode (phason), the CDW phase propagates in space, whereas in an amplitude mode (amplitudon), the CDW amplitude oscillates. When the CDW is incommensurate, phason and amplitudon dispersion relations are analogous to the ones of acoustical and an optical phonons. The phason has an oscillation energy of 0 for $q = 0$ for incommensurate CDWs and does not change the magnitude of the CDW gap, whereas the amplitudon changes the CDW amplitude and the size of the CDW bandgap periodically in time [6]. The CDW amplitude mode modulates the electronic structure in the nesting region near the Fermi wave vector k_F below the CDW phase transition temperature T_{CDW} and exhibits a characteristic mode softening upon approaching T_{CDW} [6]. It can thus be anticipated that the signature of the amplitude mode is directly observable in tr-ARPES experiments by a modulation of the CDW bandgap near k_F.

The CDW model system TbTe$_3$ is a member of a family of rare-earth tritellurides RTe$_3$, where R can be substituted with most lanthanides. RTe$_3$ is a quasi-1D model system and is well suited to the study of CDW formation [26–33]. The RTe$_3$ unit cell as depicted in figure 1(a) is constructed from the basic building block of square Te planes and buckled RTe slabs, where one RTe slab resides between two largely decoupled Te planes. Two of these building blocks are stacked up along the b-axis. The crystal structure and band dispersion of RTe$_3$ near E_F are well described in a tight-binding model [27, 32, 33] with weakly hybridized $5p_x$- and $5p_z$-orbitals of the Te-plane, as shown in figure 1(b). Since the planar square net of Te atoms is rotated through 45° with respect to the RTe slab, two different unit cells in real space are appropriate: the larger 3D unit cell is defined by the Tb atoms of the buckled slab (solid green line in figure 1(b)), whereas the smaller 2D unit cell is given by the square Te plane (dashed purple line). For the band structure in reciprocal space (see figure 1(c)), this results in a larger 2D Brillouin zone (BZ) (dashed purple line) corresponding to the Te square, which is rotated through 45° with respect to the smaller 3D BZ (solid green line). The underlying RTe bilayer with its finite 3D character reduces the BZ to $\sqrt{2} \times \sqrt{2}$-R45° symmetry and determines the diamond-like shape of the FS with quasi-1D lines that are slightly curved due to the weak hybridization perpendicular to the $5p_x$ and $5p_z$ Te orbitals [31, 32, 34]. Below the CDW phase transition temperature T_{CDW} (335 K for TbTe$_3$), the FS nesting with a nesting vector Q_{CDW} opens up a bandgap at the tip of the FS along the c-axis, indicated by dashed curves in figure 1(c). Q_{CDW} lines up with the reciprocal lattice vector c^*, is about $2/7c^*$ in magnitude, incommensurable, and believed to be nesting-driven [26, 27, 32, 35, 36]. In real space, this freezes the associated lattice vibration, which is equivalent to a displacement Δz of the ion positions (see the schematic sketch in figure 1(b)).

2. Experimental methods

The TbTe$_3$ samples were grown by slowly cooling a binary melt at Stanford University [25]. In order to perform ARPES, the samples are aligned with Laue diffractometry, which also confirms their single-crystalline quality. For the tr-ARPES measurements, the TbTe$_3$ crystals are mounted on a 45° slanted post (see figure 2(b)) in order to access the FS at $h\nu = 6$ eV (see figure 3, left panels). The samples are cleaved *in situ* at pressures better than 5×10^{-11} mbar to prepare the surface for measurement.

The tr-ARPES setup at the Freie Universität Berlin is based on a regeneratively amplified laser system (Coherent RegA 9050) and an ultrahigh vacuum (UHV) chamber, which are described in detail elsewhere [15, 37, 38]. The RegA system operates at a 300 kHz repetition
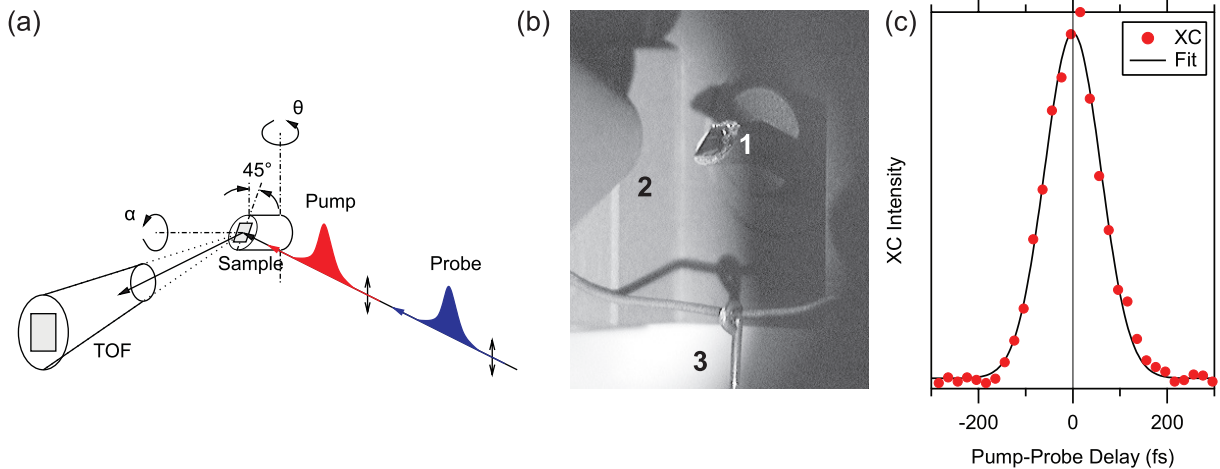
(a)

(b)

(c)

Figure 2. (a) Schematic geometry of the tr-ARPES setup, indicating the rotational degrees of freedom. Taken from [16], supporting online material. (b) Photograph of the sample (1) in front of the TOF analyzer (2). The end of the wire retaining the cleaved top post is visible (3); see text. (c) XC of the hot electron distribution at $F = 0.35\,\mathrm{mJ\,cm^{-2}}$ pump fluence integrated over $E - E_F = 1.4$–$1.5\,\mathrm{eV}$ and a Gaussian line fit, which serves as a measure of the temporal resolution and determines zero delay.

rate, $h\nu_1 = 1.50\,\mathrm{eV}$ and up to $5\,\mu\mathrm{J}$ pulse energy. Of its fundamental IR output, 60% is used to excite the sample, after further variable attenuation with a filter wheel. The UV probe pulses at $h\nu_2 = 6\,\mathrm{eV}$ and $\sim 100\,\mathrm{pJ}$ pulse energy, corresponding to $\sim 10^{13}$ photons s^{-1} ($\sim 3 \times 10^8$ photons per pulse), are generated by frequency-doubling the remaining 40% of the RegA output twice in β-bariumborate crystals and subsequent compression in prism pairs.

The IR pump pulses present a pulse duration of 55 fs, whereas the UV probe pulses are slightly longer with 80 fs due to uncompressed higher order group velocity dispersions. The cross-correlation (XC) of pump and probe pulses at $E - E_F = 1.5\,\mathrm{eV}$ results in an overall time-resolution of 100 fs (see figure 2(c)).

For the determination of zero pump–probe delay, XCs of the hot electron signal at $E - E_F = 1.4$–$1.5\,\mathrm{eV}$ are evaluated (see figure 2(c)). In this procedure, two different regimes for the decay of the hot electron signal are encountered and treated accordingly. First, at low fluences of $F \lesssim 1\,\mathrm{mJ\,cm^{-2}}$, the determination of zero pump–probe delay is straightforward since the density of hot electrons is $\ll 1\%$ of the conduction electrons near E_F. Thus, the phase space for electron–electron (e–e) scattering is not affected by the optical excitation and the excited electron population decays via e–e scattering in the limit of single-particle interactions. Under such low excitation conditions, typical hot electron lifetimes in metals amount to 2–25 fs at $E - E_F = 1.5\,\mathrm{eV}$ [18] and hence are much smaller than the width of the XC trace. This allows one to neglect the finite hot electron lifetime in the evaluation of zero delay and the pulse duration and to approximate the response function by a Dirac δ-function. This simplification is justified *a posteriori* by the symmetric XC traces (see figure 2(c)). Secondly, at larger fluences of $F \gtrsim 1\,\mathrm{mJ\,cm^{-2}}$, the excitation densities exceed 1%. This reduces the phase space available for e–e scattering as secondary electrons populate the energy interval of interest at later times [39]. This results in a fluence-dependent decrease in the observed hot electron relaxation rates. For
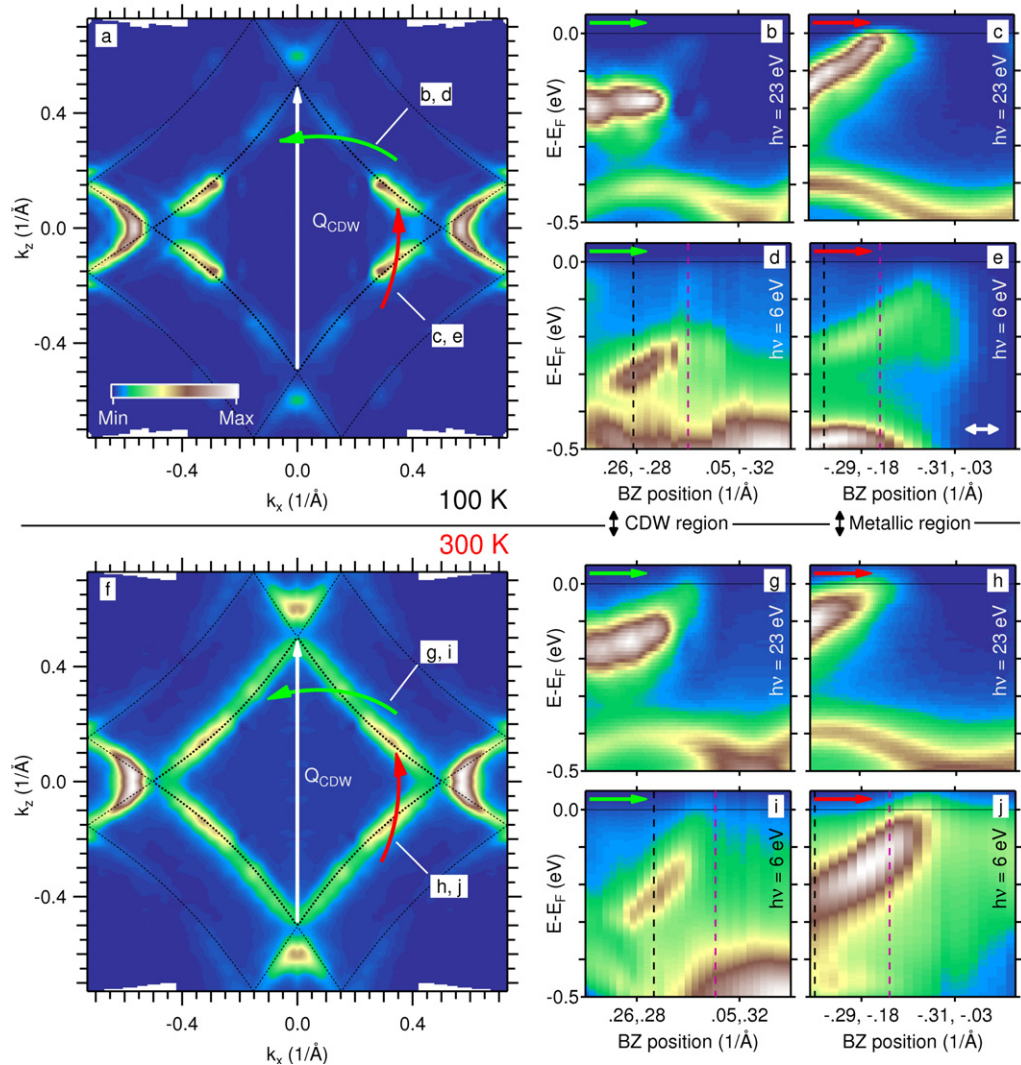
Figure 3. The FS of TbTe3 at 100 K (a) and 300 K (f) is obtained by integration of the photoemission intensity over an energy window of 20 meV width centered around E_F. At 300 K, the CDW gap is almost closed. The CDW nesting vector Q_{CDW} (white arrow) and the paths of the band dispersion through the FS in the ungapped metallic region (red arrow) and the gapped CDW region (green arrow) are indicated. The bold and thin dashed lines indicate the FS and the back-folded bands, respectively, calculated within a tight-binding approximation [27, 32, 33]. Panels (b), (d) and (g), (i): band dispersion in the gapped region at 100 and 300 K, respectively. Panels (c), (e) and (h), (j): band dispersion in the ungapped region at 100 and 300 K, respectively. Measurements at $h\nu = 6$ eV are acquired with the tr-ARPES setup without IR excitation, while those at $h\nu = 23$ eV are measured with a conventional ARPES setup. The vertical black and purple dashed lines in (d), (e), (i) and (j) indicate the positions at which time-resolved data were taken (cf figures 4 and 6). The white arrow in panel (e) indicates the TOF acceptance angle. For the curved cuts presented in panels (b)–(e) and (g)–(j), the BZ position is given in pairs of k_x, k_y coordinates. The intensity scale used for all false color plots in this figure and throughout this paper is seen in the inset of panel (a).

the evaluation of zero delay and the pulse duration, these apparent lifetimes were taken into account. The time-correlated pairs of femtosecond pump and probe laser pulses, $h\nu_1$ and $h\nu_2$, respectively, are focused into the UHV chamber and spatially overlapped on the sample surface.

Typical pump fluences are of the order of $F = 0.35$–$3\,\mathrm{mJ\,cm^{-2}}$ and below the damage threshold of TbTe$_3$ as no irreversible spectral changes were encountered. At pump fluences above $F \geqslant 1\,\mathrm{mJ\,cm^{-2}}$, the photoelectron count rate from only the IR pump pulse increases nonlinearly to up to 15 kHz at $3\,\mathrm{mJ\,cm^{-2}}$. The fluence of the 6 eV probe pulse is adjusted so that the spectral broadening due to space charging is below the spectrometer resolution of 10 meV, resulting in typical count rates of 200–400 kHz.

The binding energy of the photoemitted electrons is determined from their kinetic energy E_{kin} analyzed in a time-of-flight (TOF) spectrometer: $E - E_{\mathrm{F}} = E_{\mathrm{kin}} + \Phi - h\nu$. Here, Φ denotes the spectrometer work function and $h\nu = h\nu_2$ the photon energy of the probing UV laser pulse. The work function of TbTe$_3$ was determined to be around $5.23 \pm 0.1\,\mathrm{eV}$.[8] Biasing the sample compensated for the work function difference between the sample and the spectrometer in order to avoid electrostatic fields that would affect the angular distribution of the photoemitted electrons. The spectrometer with an acceptance angle of $\pm 3.5°$ features an energy resolution of $\sim 10\,\mathrm{meV}$ at $E_{\mathrm{kin}} = 1\,\mathrm{eV}$. The photograph in figure 2(a) shows how the (cleaved) sample is placed $\sim 3\,\mathrm{mm}$ in front of the TOF spectrometer opening.

As a reference, we also carried out conventional high-resolution ARPES measurements at beamline 5–4 at the Stanford Synchrotron Radiation Laboratory with a similar UHV chamber and sample preparation system, but without slanted posts. A Scienta R4000 hemispherical electron analyzer with a total energy resolution of 10 meV and an angular resolution of better than 0.3° is used in this experiment. In the synchrotron-based experiments, we used a photon energy of 23 eV, as in previous studies [27, 32, 33].

The schematic tr-ARPES measurement geometry is shown in figure 2(a). For a given sample orientation, the manipulator angle Θ is rotated, yielding a series of measurements that constitute a path through the BZ, which reveals the band dispersion (see figure 3). The samples are mounted on 45° slanted posts to shift the accessible BZ region away from the $\bar{\Gamma}$-point and enable measurements at TbTe$_3$ at $h\nu = 6\,\mathrm{eV}$. Due to the limited BZ access in the tr-ARPES experiments at such low photon energies, only a curved path through either the gapped or the ungapped region is accessible by taking multiple measurements while rotating around Θ (cf figure 2(a)). The Laue diffraction we used for sample orientation before the measurements cannot distinguish between the lattice a and c vectors since they are nearly identical [25, 26]. Therefore, two consecutive ARPES measurements are obtained from the same sample: first, the sample is cleaved and the band dispersion is measured for $T \ll T_{\mathrm{CDW}}$ and for $T \approx T_{\mathrm{CDW}}$. Then, the top post, which is retained by a Ta wire (see figure 2(a)) and holds a second part of the same sample, is carefully rotated through 90° along α, glued on a slanted sample post, cleaved and the measurement at the above two temperatures is repeated in a second experiment. This approach allows us to access both the gapped and the ungapped parts of the BZ from the same sample.

The strength of conventional ARPES setups in combination with synchrotron light sources is the excellent angle- and energy-resolution and a tunable photon energy. This enables access to the entire BZ and choosing appropriate photon energies. On the other hand, the introduction of femtosecond time resolution into ARPES opens up a new field for the study of collective excitations, especially the effects of electron–boson coupling, in real time. However, the

---

[8] We measured the work functions on two of our samples to be $5.33 \pm 0.03\,\mathrm{eV}$ and $5.13 \pm 0.03\,\mathrm{eV}$, respectively.

bandwidth of the femtosecond laser pulses of several 10 meV limits the energy resolution. However, as we shall see later, this restriction only applies to frequency domain properties such as the (equilibrium) electron band width, but to a much lesser degree to time domain properties such as coherent oscillations. Hence, it is important to achieve a sufficiently high signal-to-noise ratio that allows us to detect very small changes in the transient spectra. This requires a careful trade-off between the acceptance angle and the transmission of the spectrometer. The currently employed UV photon energy of 6 eV also limits the accessible BZ. However, the ongoing development of femtosecond high-harmonic light sources [21, 22] might lift the limitation to low photon energies in the near future. In this respect, the current state-of-the-art ARPES and tr-ARPES experiments provide complementary information because they are optimized for measurements in the frequency and time domains, respectively.

3. Results

We begin with a discussion of the band structure of TbTe$_3$ in thermal equilibrium. Figures 3(a) and (f) show color-coded plots of the photoemission intensity at E_F probed by conventional ARPES at $h\nu = 23$ eV. The data reveal the diamond-shaped FS of TbTe$_3$, which is highlighted by the bold and thin dashed lines that indicate the FS and the back-folded bands calculated within a tight-binding approximation [27, 32, 33]. The FS in figure 3(a) was measured at 100 K and presents a band gap due to the FS nesting by the CDW vector Q_{CDW}. The FS in figure 3(f) was acquired at 300 K, near $T_{CDW} = 335$ K [26], and indicates an almost entirely closed CDW bandgap, which is in agreement with previous works [27], [32–34].

In the right panels of figure 3, we compare the band dispersion measured with the ARPES and tr-ARPES setups to investigate the CDW bandgap in more detail. The cuts through the BZ along curved paths defined by the tr-ARPES geometry are indicated by red and green arrows in figures 3(a) and (f). The conventional ARPES data are interpolated along these paths. In general, the ARPES data at $h\nu = 23$ eV and $h\nu = 6$ eV agree well near E_F, although some deviations are encountered for lower-lying bands. Since the two data sets were obtained with two different photon energies in different experimental geometries, these deviations could have several origins. The photoemission matrix elements and cross sections are different. Furthermore, changes in escape depth lead to different surface/bulk sensitivities for the two light energies. Lastly, final state effects might be more pronounced at lower photon energies.

Focusing on the upper band dispersing from $E - E_F \approx -0.25$ eV to E_F, its band dispersion in figures 3(b) and (d) clearly exhibits a CDW bandgap in the CDW nesting region at 100 K. This is in contrast to the continuous dispersion of the conduction band through E_F in figures 3(c) and (e), taken in the ungapped region, not nested by Q_{CDW}. At 300 K, where the CDW bandgap has almost closed, figures 3(h) and (j) show very little change in the band dispersion in the *ungapped* ('metallic') region except for thermal broadening. On the other hand, the band dispersion in the *gapped* ('CDW') region in figures 3(g) and (i) has changed qualitatively and disperses through E_F. This qualitative difference of the temperature-dependent dispersion allows one to unambiguously assign the two sets of ARPES measurements to the gapped and the ungapped region of the FS. The dispersion in the CDW nesting region is characterized by a bandgap that closes with increasing temperature, whereas the metallic region exhibits bands that cross E_F independent of temperature.

All band dispersions in figures 3(b)–(e) and (g)–(j) present the strongly temperature-dependent conduction band and a weakly dispersing band at about 0.5 eV binding energy.

Neglecting the CDW bandgap, the conduction band can be described well by a tight-binding model of $5p_x$ and $5p_z$ Te orbitals [27, 32, 33]. Conversely, the weakly dispersing band at $E - E_F \sim -0.5$ eV cannot be matched well to the tight-binding model. Local density approximation (LDA) calculations [31] can be scaled and shifted to agree with this lower band [27], but this agreement is limited to a small region in the BZ. This might be because the LDA calculation neglects the rare-earth $4f$ orbitals. In order to fully reproduce the ARPES data, it would be desirable to perform an LDA+U calculation, which takes into account the orbital dependence of the Coulomb and exchange interactions between the $4f$ orbitals that are absent in LDA. This approach is suited for correlated materials, would include the rare-earth $4f$ electrons and would reproduce their energy levels more appropriately. Such a calculation is currently under investigation. In short, the lower-lying, weakly dispersing band cannot be directly assigned to any specific orbital, but might be of Te $5p_y$ character with some overlap of a Tb $4f$ orbital. Henceforth, we will refer to the two bands as the upper band or CDW band and the lower band.

A priori, the reasonable correspondence the ARPES data at $h\nu = 23$ eV between and $h\nu = 6$ eV is not self-evident, since the photoemission signal might differ due to energy-dependent matrix elements and a different escape depth of the photoelectrons. The good agreement between the two experiments observed here ensures that the same position in the BZ is probed in tr-ARPES as in conventional ARPES. Thus, the collective excitations in TbTe$_3$ can safely be analyzed with tr-ARPES in the following.

3.1. Dynamics in the ungapped region

We now turn to the tr-ARPES measurements and begin with a discussion of transient ARPES spectra recorded in the *ungapped* region of the FS. With this data, we establish a direct comparison with the dynamics observed in the *gapped* CDW region. This systematic approach allows us to draw further conclusions about the underlying e–ph coupling as an ingredient of the CDW mechanism and its fundamental collective excitations.

Figure 4 shows the color-coded photoemission intensity as a function of binding energy and pump–probe delay for 300 and 100 K at different locations in the BZ, as indicated in figures 3(e) and (j). Before we turn to the coherent dynamics of the occupied states, we briefly discuss the dynamics of the excited electron distribution above E_F. At a pump–probe delay of 0 fs, the photoemission intensity above E_F increases since the IR pump pulse generates excited electrons due to electron–hole (e–h) pair excitation. After ~ 200 fs, the distribution function has significantly broadened because the initially non-thermal electron distribution thermalizes due to e–e scattering, resulting in an equilibrated electron distribution with elevated electron temperature [40]. On a timescale of a few ps, the intensity above E_F decreases and the Fermi edge regains sharpness as the hot electron distribution relaxes via e–ph scattering and transfers energy to the lattice. We detect this behavior in all transient spectra of TbTe$_3$. These processes can be rationalized by the two-temperature model [40] and are typically observed in metals that have been photoexcited by intense femtosecond laser pulses [15].

Turning to the dynamics in the occupied part of the band structure, we note that the pump-induced variations do not exhibit qualitative changes as a function of temperature, nor as a function of position in the BZ, where the upper band disperses below k_F (figures 4(a) and (c)) or at k_F (figures 4(b) and (d)). Focusing on the transient binding energies, two effects are visible in all spectra of figure 4: the upper band shifts towards E_F, i.e. lowers its binding
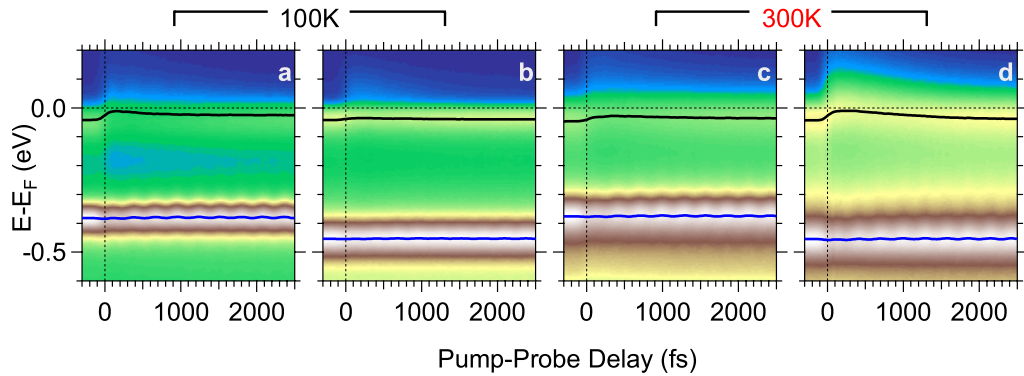
Figure 4. Momentum dependence of the photo-induced excitations in the ungapped metallic region of TbTe$_3$. Time-dependent photoemission intensity as a function of binding energy for an incident pump fluence of $F = 2.6\,\mathrm{mJ\,cm^{-2}}$ and $T = 100$ and $300\,\mathrm{K}$. The solid lines indicate the transient binding energy obtained from Lorentzian line fits of the upper band at $E - E_F = -0.05\,\mathrm{eV}$ and the lower band at $E - E_F \approx -0.5\,\mathrm{eV}$; see text and figure 5. The BZ locations of (a) and (b) are indicated by the vertical black and purple dashed lines in figure 3(e), and the locations of (c) and (d) are indicated by the vertical black and purple dashed lines in figure 3(j), respectively.

energy. Furthermore, we are able to resolve periodic variations of the energy and intensity of the lower band. These oscillations are attributed to a coherent collective excitation of the coupled electron–lattice system as we detail in the following.

In order to examine the transient binding energy changes quantitatively, the time-dependent spectra are fitted with two Lorentzians, one for each of the two observed bands. This description is justified as long as the pump-induced changes are small so that the Lorentzian line shape is retained at all delays, which we found verified for the spectra in the ungapped region.

Figures 5(a) and (d) show the resulting transient binding energy changes ΔE in the ungapped region for the CDW band and the lower band, respectively. As evident from the raw data in figure 4, the CDW band responds to the laser excitation by shifting 5–35 meV towards E_F, which occurs on the timescale of the laser pulse duration of 100 fs. Subsequently, ΔE relaxes within a few ps, but, without fully recovering after 5 ps. The distinct timescales for the rise and decay of ΔE allow one to disentangle the fundamental interactions during and after ultrafast laser excitation: the 100 fs timescale for the rise in ΔE suggests that the initial binding energy shift is driven by the e–h pair creation due to the IR pump laser pulse and the resulting change in the electronic energy landscape. The subsequent energy relaxation can be fitted by a double exponential decay, as shown exemplarily by the solid green line in figure 5(d). The first decay constant ranges from 0.4 to 1 ps and the second decay constant amounts to several ps.

In contrast to the hot electron dynamics of the CDW band, the dynamics of the lower band are governed by a pronounced coherent mode (see figure 5(d)). Note that the lower band exhibits not only oscillations of ΔE but also oscillations of amplitude and width of the Lorentzian line (not shown). This mode is analyzed by Fourier transformation (FT) of ΔE, as shown in figures 5(b) and (c). The FT indicates a pronounced coherent mode at 3.5(5) THz. The CDW band does not show the binding energy oscillations as clearly and a double exponential background (see solid green line in figure 5(a)) was subtracted prior to the Fourier analysis.
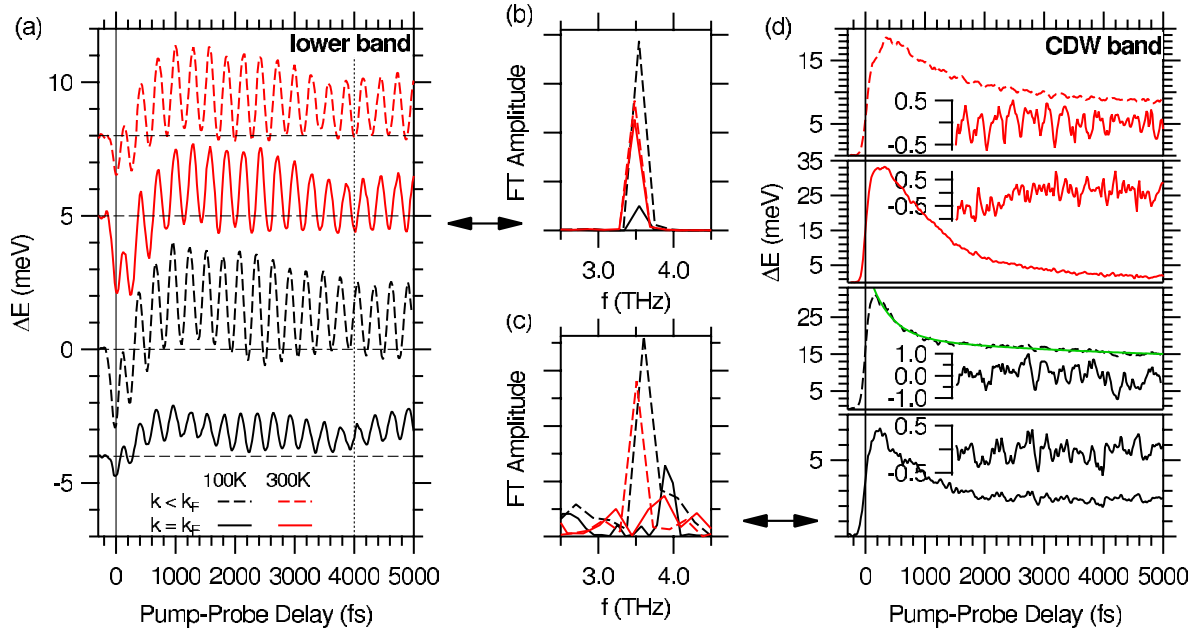
Figure 5. Transient binding energy changes, ΔE, from the Lorentzian line fits of the tr-ARPES data in figure 4 (i.e. in the ungapped region). (a) The transient binding energy change in the lower band reveals coherent oscillations. For clarity, the traces have been offset. (d) At 0 fs, the binding energy of the upper band shifts towards E_F on the timescale of the laser pulse duration of 100 fs and subsequently recovers. The solid green line indicates a double exponential fit; see text. The respective insets show the magnified, background-subtracted data in order to visualize the oscillations more clearly. (b, c) FTs of the transient binding energies of the lower and CDW bands, respectively, taken after a pump–probe delay of 0.5 ps. The oscillations in the upper and lower bands exhibit a comparable frequency of 3.5(5) THz and do not depend systematically on temperature and position in the BZ.

The oscillations track the same mode at 3.5(5) THz observed in the lower band. The collective mode at 3.5 THz, which is most clearly observed in the lower band, does not depend on the details of the probed BZ region, temperature and binding energy of the band. This points to the 3.5 THz mode being a coherent phonon of $TbTe_3$, similar to what has been reported for other materials before [15], [41–43]: it is a 'generic' lattice vibration; that is to say, it does not seem to have any ties to CDW physics. Interestingly, the dynamics of the CDW band are governed by the incoherent hot electron dynamics, and the weak coherent oscillations in the CDW band are close to the detection limit. In contrast, the dynamics of the lower band are dominated by coherent oscillations and binding energy shifts due to incoherent processes are negligible. At least qualitatively, this distinct response can be understood by the different binding energies of the bands: the CDW band is close to E_F and thus more susceptible to e–h pairs excited by laser excitation and subsequently created secondary electrons and holes. For the same reason, the lower band with its higher binding energy is less affected by the hot electron population. On the other hand, the pronounced coherent oscillations in the lower band suggest a stronger coupling
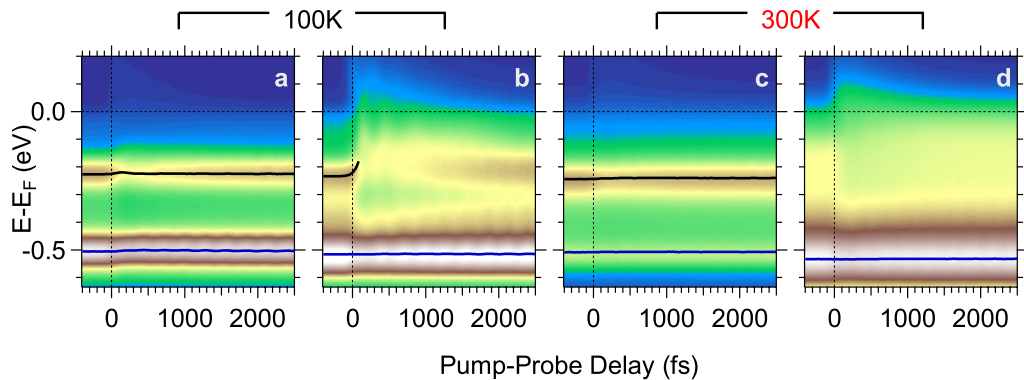
Figure 6. Momentum dependence of the electronic excitations in the gapped CDW region of TbTe$_3$. Time-dependent photoemission intensity as a function of binding energy for an incident pump fluence of $F = 2.6\,\mathrm{mJ\,cm^{-2}}$, and $T = 100$ and 300 K. In contrast to the ungapped metallic region (see figure 4), the response of the CDW band depends strongly on the BZ position and is maximal for $k = k_F$. The solid lines indicate the transient binding energy obtained from Lorentzian line fits of the upper band at $E - E_F \approx -0.25\,\mathrm{eV}$ and the lower band at $E - E_F \approx -0.5\,\mathrm{eV}$. The line fit for the upper band is only displayed where such a fit was possible. The BZ locations of (a) and (b) are indicated by the vertical black and purple dashed lines in figure 3(d), and the locations of (c) and (d) are indicated by the vertical black and purple dashed lines in figure 3(i), respectively.

to the lattice mode at 3.5(5) THz, which might be related to the symmetry of the electronic wave function and the phonon mode.

3.2. Dynamics in the gapped charge-density wave (CDW) region

We now focus on the gapped CDW region in order to compare it to the dynamics of the ungapped region of the BZ. The data were obtained from the same sample after rotation by 90° (see section 2) under identical experimental conditions.

Figure 6 shows tr-ARPES spectra at 100 and 300 K taken at BZ positions indicated in figures 3(d) and (i) for a pump fluence of $F = 2.6\,\mathrm{mJ\,cm^{-2}}$. The striking difference between the gapped and ungapped BZ regions is the response of the upper CDW band to the laser excitation. As shown in figures 6(a) and (c), the pump-induced band shift, band depletion, and change in band shape is similar to the metallic region for $k < k_F$ (compare with figure 4). This is in contrast to the significantly larger response when the CDW band is at k_F (see figures 6(b) and (d)): the hot electron density above E_F increases notably. The CDW band shifts towards E_F and its spectral weight is redistributed strongly, weakening the band intensity. The band intensity, width, Lorentzian shape and amplitude slowly recover for delays > 1 ps. For $k = k_F$ and 100 K (figure 6(b)), the CDW band exhibits a new collective excitation mode strongly disturbing the CDW band. The modulations of the lower band, however, resemble those of the ungapped region, regardless of BZ position. A quantitative analysis is presented in the following, where we consider the pump fluence dependence of these pump-induced transient changes.
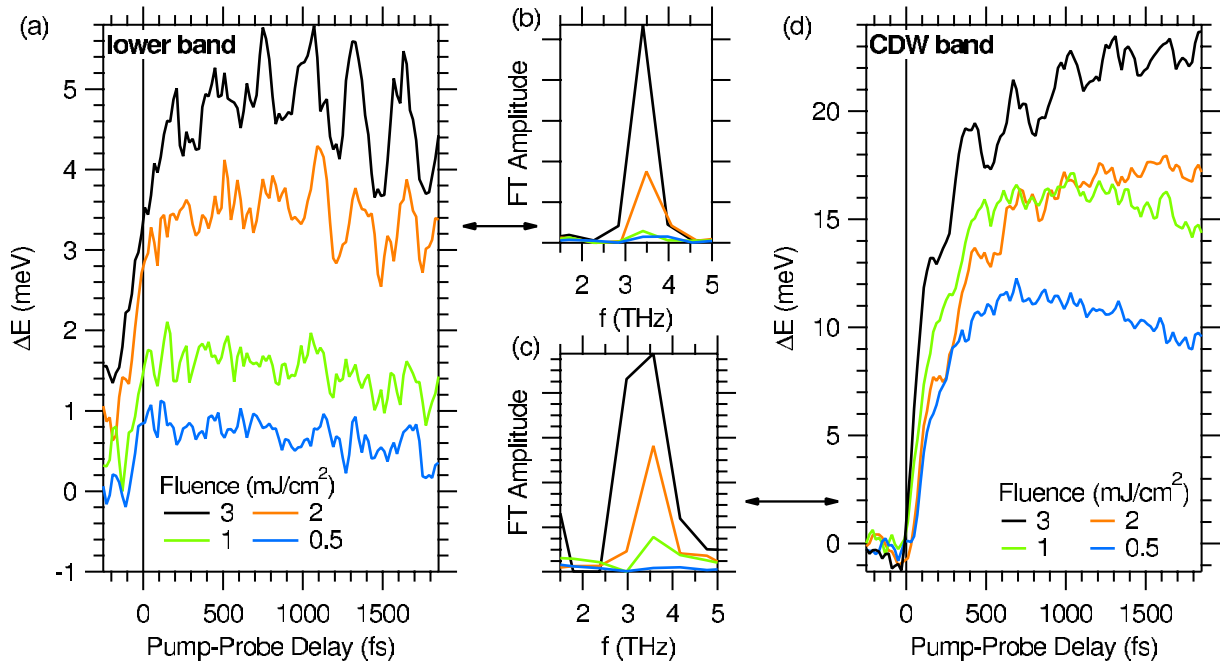
Figure 7. The transient binding energy changes, ΔE, in the CDW region at 300 K for the lower (a) and the upper (d) CDW band were derived from Lorentzian line fits for different incident fluences. For clarity, the data in (a) have been offset. Panels (b) and (c) depict FT of ΔE for delays > 200 fs after subtraction of a smooth background function. The dominant mode at 3.5(5) THz is independent of the excitation density and binding energy of the band.

3.2.1. Fluence-dependent relaxation dynamics in the gapped region. Next, we present evidence for the phase coherent excitation of the CDW amplitude mode and closing of the CDW bandgap by analyzing the transient binding energies at k_F in the CDW nesting region as function of excitation density. This systematic study enables us to gain further insights into the transition between weak perturbations, which feature small responses and excite collective modes in the CDW band, and strong perturbations, which drive the transition from the gapped CDW state to a metal-like ungapped state.

Figures 7(a) and (d) depict the transient binding energies, ΔE, of the lower and the upper CDW band, respectively, as a function of incident pump laser fluence at 300 K. ΔE has been extracted by Lorentzian line fits, as described in section 3.1. The overall behavior of ΔE at 300 K is similar to the data from the ungapped region (compare with figure 5). Turning to the coherent excitations, a coherent mode at 3.5(5) THz is observed in the lower band as well as in the CDW band, being phase-locked with respect to the lower band. The quantitative analysis is performed by FT of ΔE for delays > 200 fs after subtraction of a smooth, phenomenological background. The background describes incoherent contributions to transient heating of the electron and phonon subsystems [15, 23]. The oscillation amplitude in both bands increases monotonically with excitation density, as seen from the FT amplitudes in figures 7(b) and (c). Although ΔE exhibits a high statistical background, the oscillations are clearly resolved, even for oscillation amplitudes of < 1 meV, which are one order of magnitude below the nominal instrumental energy resolution of 10 meV. The high degree of similarity displayed

in all transients and the smooth change in the oscillation amplitude with fluence—while the phase of the oscillations remains at the same delays—proves that our sensitivity is $< 1\,\text{meV}$. This is because the fitting of the transient spectra for many consecutive delays allows a highly systematic extraction of the Lorentzian line parameters.

Interestingly, a 2.5 THz mode, which we will discuss to be the amplitude mode of the CDW, is not detected at 300 K in the CDW nesting region. This is not immediately obvious since at $300\,\text{K} < T_{\text{CDW}} = 335\,\text{K}$ the CDW amplitude mode should in principle still be present and detectable. However, since the excitation densities are sufficient to drive an ultrafast transition from the CDW state to an ungapped transient state at an equilibrium temperature of 100 K—significantly below T_{CDW}—it is plausible that near T_{CDW} at 300 K, even the lowest pump fluence excites the system out of the CDW state and thus quenches the CDW amplitude mode. Alternatively, this mode could be so weak at 300 K that it eludes detection. Therefore, the transition between high and low pump fluences is best studied at temperatures significantly below the phase transition temperature.

Figure 8 shows the photoemission intensity as a function of pump–probe delay and binding energy at k_{F} and 100 K for various fluences. These data present a systematic, fluence-dependent crossover between a strongly excited regime (figures 8(a)–(c)), which drives an ultrafast transition from the gapped CDW state to a transient metallic state, to a weak excitation regime, in which collective oscillations in the CDW band are detected (figures 8(d) and (e)). As a function of excitation density, the transient CDW band position shifts towards E_{F} and the bandwidth broadens significantly for the three largest fluences (see figures 8(a)–(c)). The response changes towards lower fluences, depicted in figures 8(d) and (e), where the shift and broadening are significantly less pronounced. Before we proceed to further evaluate the data in figure 8, we would like to point out that all coherent modes presented henceforth already reveal themselves in a striking manner in the raw data; frequencies can be determined by counting the temporal peak distances.

A quantitative analysis concerning the CDW band shift and the bandwidth turns out to be difficult. The transient binding energy shift of the CDW band is one to two orders of magnitude larger than the superimposed coherent oscillations. The electronic system—especially at high fluences—is far out of equilibrium and the decay does not follow simple exponentials, precluding a background subtraction for the frequency analysis prior to FT. Also, the CDW band becomes asymmetric and deviates strongly from a simple Lorentzian line shape. Therefore, in the following analysis of the CDW band position, we avoid specific assumptions about the line shape and employ a center-of-mass analysis, while using a Lorentzian line for the lower band. Furthermore, a Fourier analysis might present difficulties as the high excitation densities are well known to lead to shifts in the frequency Ω, which then becomes time dependent due to anharmonic effects [17].

In figure 9, we present the time-dependent binding energy determined by Lorentzian fits for the lower band and the center-of-mass analysis for the CDW band. The oscillation amplitude in the lower band (figure 9(a)) increases continuously with increasing pump fluence. Phase and frequency remain the same throughout the entire fluence range. Thus, the response of the lower band at 100 K is similar to the corresponding data at 300 K (compare with figure 7(a)). The FTs for the lower band (figure 9(c)) consistently show a peak at 3.5(5) THz and are comparable to the 300 K data (see figure 7(b)). These results confirm the assignment of the 3.5 THz mode being a generic coherent phonon of TbTe$_3$ since no pronounced dependence on the temperature, BZ position and excitation density is observed.
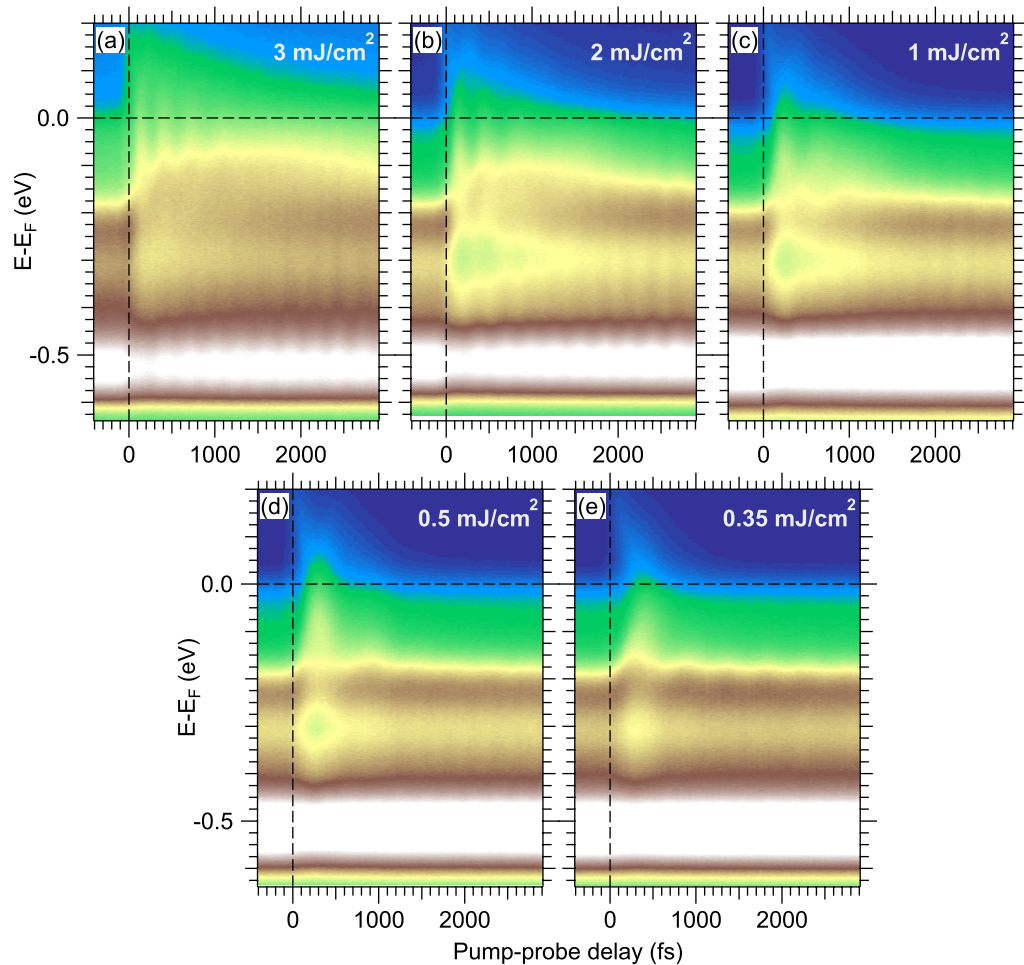
Figure 8. Photoemission intensity as a function of binding energy and pump–probe delay at various pump fluences ranging from $3\,\mathrm{mJ\,cm^{-2}}$ (a) to $0.35\,\mathrm{mJ\,cm^{-2}}$ (e). (a–c) Strongly perturbative regime that transiently melts the CDW state. (d, e) Weakly perturbative regime in which the CDW amplitude mode is observable.

This is in marked contrast to the fluence- and temperature-dependent response of the upper CDW band shown in figure 9(b). In comparison to the data at 300 K (see figure 7(b)), the decay time of the binding energy shift ΔE strongly depends on the excitation density and increases with increasing fluence. The superimposed coherent oscillations present a complex behavior that depends on fluence and pump–probe delay. For the lowest fluence of $0.35\,\mathrm{mJ\,cm^{-2}}$, the period of the oscillations, as indicated by vertical lines in figure 9(b), is essentially constant as a function of delay and amounts to $\tau = 480(50)\,\mathrm{fs}$, corresponding to a frequency of $f = 1/\tau = 2.1(2)\,\mathrm{THz}$. The situation becomes more complicated at an intermediate fluence of $1\,\mathrm{mJ\,cm^{-2}}$, where no oscillation of a clear single frequency is discernible. For the largest fluences of $3\,\mathrm{mJ\,cm^{-2}}$, the oscillation period depends on the pump–probe delay: the oscillation periods increase with increasing delay from 240(50) fs (4.2(9) THz) for the first to 300(50) fs (3.3(6) THz) for the second and 400(50) fs (2.5(4) THz) for the third oscillation. The subsequent oscillations are again shorter and constant with a period of 280(50) fs (3.6(7) THz). The response
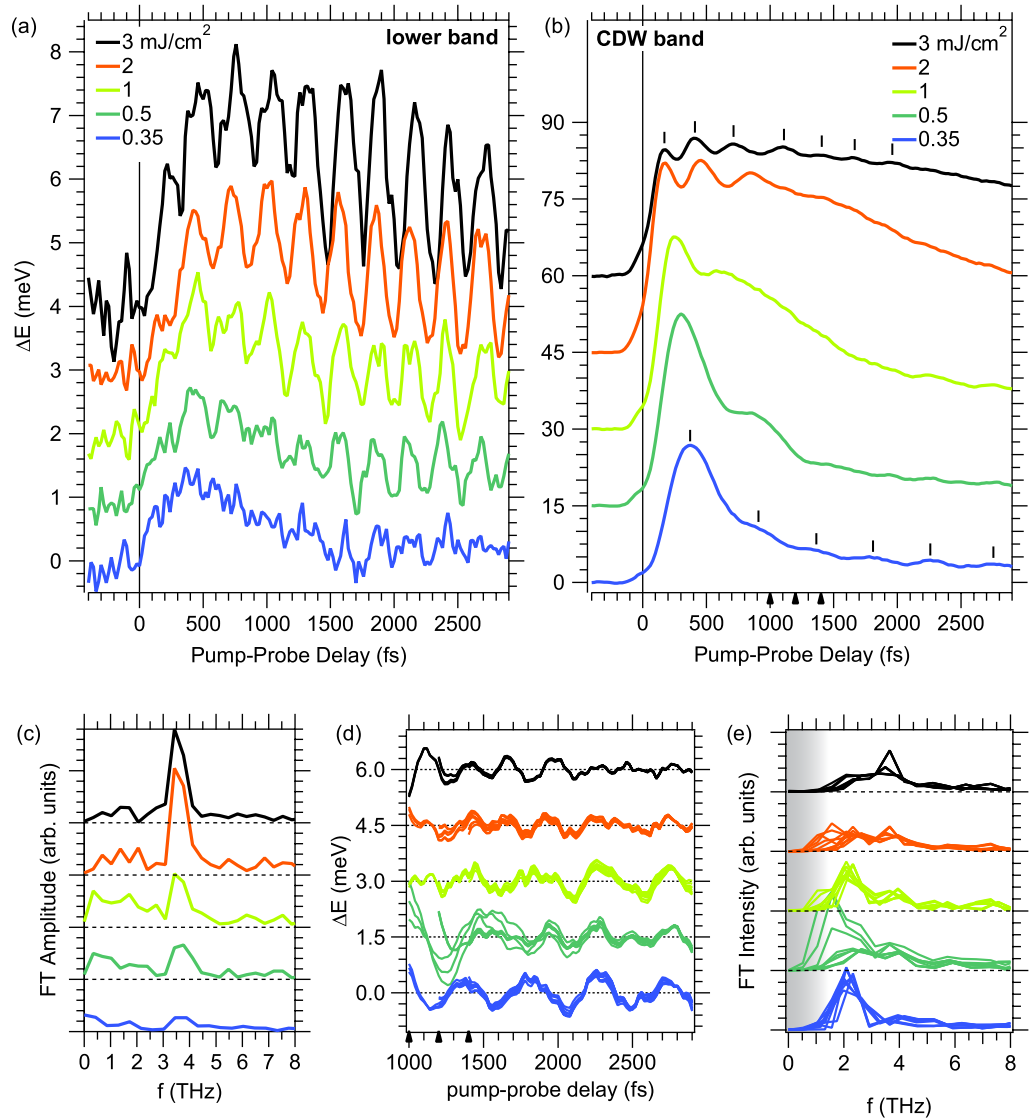
Figure 9. Fluence-dependent transient binding energy changes ΔE in the CDW region at 100 K for the lower (a) and the upper (b) CDW band are derived from a Lorentzian line fit and a center-of-mass analysis, respectively. For clarity, the traces in panels (a) are offset by 1 meV and the ones in (b) by 15 meV. The peak maxima of the coherent mode in (b) are indicated (vertical lines). Panel (c) depicts FT of ΔE for delays > 500 fs of the lower band plotted in (a). Panel (d) shows the oscillations of the upper band displayed in (b) after background subtraction (see text). Panel (e) plots the FTs of the background-subtracted center-of-mass of the upper band displayed in (d). For each fluence dependence, panels (d) and (e) show the results of background subtraction with different choices of the cutoff time (black arrows in (b) and (d)) and number of spline nodes (see text). The spectral intensity is suppressed towards zero frequency by the background subtraction (grayed region). While the lower band is dominated by a 3.5(5) THz coherent mode at all fluences, the CDW band exhibits a collective mode at 2.5(5) THz at low fluences and a 3.5 THz mode emerges for increasing pump fluences.

of the CDW band showcases the transition between CDW melting at high fluences and a more gentle excitation that results in the observation of a new mode in the CDW band.

Fourier transforming the transient binding energy of the CDW band turns out to be challenging. Ideally, one would determine a smooth background from the data, subtract the background and Fourier transform the result. Sometimes, exponentially decaying functions resulting from decay rate equations constitute a good choice for a background function [24]. But since the pumping drives the CDW transition and therefore pushes the system into a highly excited state, it is not surprising that exponentials do not provide a good background subtraction. Moreover, the strong fluence dependence and the non-analytical behavior of ΔE do not point to an obvious choice for a smooth background function. Certainly, a great deal of interesting physics is hidden in this incoherent background; electron–electron and electron–phonon scattering as well as transport effects contribute to thermalization and equilibration [44]. However, the electron–phonon scattering also contains CDW physics that contributes significantly. It will certainly be interesting to see what insights will be gained by theoretically modeling the relaxation dynamics, but this is beyond the scope of this paper, and we will focus more on the coherent oscillations. In order to extract these, we implement data processing techniques common to the field of extended x-ray absorption fine structure (EXAFS) [45], since this field is faced with the same challenge of having to extract oscillations superimposed on an edge, which rises at least an order of magnitude higher than the amplitudes of the oscillations.

Lee *et al* [45] describe the EXAFS data analysis procedure and suggest fitting a spline or B-spline to the data with a χ^2 test and then using that for background subtraction. The data treated thus are subsequently zero-padded and then Fourier transformed, after which a band pass filter is applied in Fourier space and the result then back-transformed. The obtained, filtered data are finally analyzed. Here, we only apply a cubical spline-fitted background subtraction and the FT (without zero padding[9]). Lee *et al* also mention that fitting a single polynomial to the entire data range does not work well because it introduces systematic errors in the FT [45], which we confirm for our data.

In order to see how stable the obtained FTs are with respect to the background subtraction, we performed the background subtraction for different time intervals starting between 600 and 1400 fs and ending at 2900 fs, and for cubical splines with 5, 6 and 7 nodes distributed evenly in the time interval. The FTs became stable only for start times $\geqslant 1000$ fs. The resulting background subtracted transient binding energy change for the upper CDW band is plotted in figure 9(d) for different time intervals $\geqslant 1000$ fs and the mentioned node numbers, and the resulting FTs are shown in figure 9(e). The fact that the FTs stop changing only for time intervals starting at $\geqslant 1000$ fs becomes more plausible considering the following. First, at the highest pump fluence, the frequencies do not remain constant during the first three or four oscillation periods (cf figure 9(b)). This is related to the second point; the system needs time for the electrons to thermalize and possibly for the CDW state to melt, during which the system is highly nonlinear and anharmonic. Here we note that, consistently, for the lowest fluence, the FT remained stable for time intervals starting as low as 600 fs (not shown). Thirdly, from a technical point of view, the traces become less smooth the closer one approaches the sharp rising edge at zero pump–probe delay, making it harder and harder to fit a well-behaved spline.

---

[9] Even though zero padding smoothes the FT, it does not actually increase frequency resolution and can furthermore introduce artifacts, such as the picket-fence effect. We found that zero padding does not reveal any more information than what the unpadded spectrum already shows.

The oscillations are clearly visible in the background-subtracted data (cf figure 9(d)), and so is a change in frequency when proceeding from lowest to highest fluences (cf figure 9(e)). The different background subtractions and FTs are relatively stable except for the curve at $0.5\,\mathrm{mJ\,cm^{-2}}$ fluence.

While not being able to capture the dependences of the frequencies on pump–probe delay, especially in the first $\approx 1\,\mathrm{ps}$, the FTs do reveal pump fluence-dependent changes on the frequency spectrum. In agreement with the analysis of the oscillation periods above, the FTs in figure 9(e) exhibit a peak at 2.5(5) THz for the lowest fluences. When going to higher fluences, a peak at 3.5(5) THz starts to emerge, while the peak at 2.5(5) THz slowly loses intensity and almost vanishes at the highest fluence. This hints at the 2.5 THz mode being intimately connected to the CDW state: it is only observed at low temperatures $T \ll T_{\mathrm{CDW}}$, in the CDW nesting region of the BZ and low excitation densities, where the CDW state is not driven into a transient metallic state.

A note about final state effects seems appropriate at this point. Due to the fact that the data have been obtained under a large angle away from the surface normal (about 45° due to the slanted sample post mentioned earlier), surface refraction of the detected electrons can play a role. A periodic modulation due to a coherent mode can modulate the final state energy and emission angle as well. However, these final state modulations would show up equally in the entire energy range measured. The fact that we observe different oscillation frequencies in different bands in the same data set cannot be explained by this kind of final state modulation.

3.3. The CDW gap around E_{F}

The technique of tr-ARPES not only allows us to measure the transient spectral function but also probes transiently populated states above E_{F} due to the pump excitation, comparable to two-photon photoemission (2PPE) experiments [44, 46]. At probe times immediately after pumping, ionic rearrangements and strong electron–electron correlations are neglected. Then, the populated states above E_{F} closely resemble states that are unoccupied in equilibrium. As the system dissipates the stored excitation energy, the potential energy surface changes. Therefore, the probed states below and above E_{F} depart from the equilibrium configuration and provide information about the relaxation dynamics.

Figure 10 shows spectra at the CDW gap maximum for different pump–probe delays to illustrate how the CDW gap evolves after pumping. At zero pump–probe delay, the peaks of the lower and upper parts of the CDW gapped band are indeed clearly visible. In agreement with previous work [27], the CDW gap amounts to 0.40 eV. For the lowest fluence (cf figure 10(d)), the occupied and the unoccupied part of the CDW band remain visible for delays $\geqslant 200\,\mathrm{fs}$. The band positions of the occupied and unoccupied CDW bands move slightly towards E_{F} with time. A Lorentzian fit of the occupied and unoccupied CDW bands (not shown) confirms that at the lowest fluence, the unoccupied CDW band position shifts downwards by 60 meV and the occupied CDW band position shifts upwards by 25 meV in the first 200 fs. After 500 fs, spectral intensity is detected at E_{F} while the unoccupied CDW band is not visible anymore since the excited electrons have formed a Fermi–Dirac distribution with elevated temperature through e–e scattering.

Note, however, that the occupied part of the CDW band decreases only slightly in intensity over time, while simultaneously intensity at E_{F} increases. This could represent a mixed state where the CDW gap is closed, while the CDW peak has changed only little in binding energy.
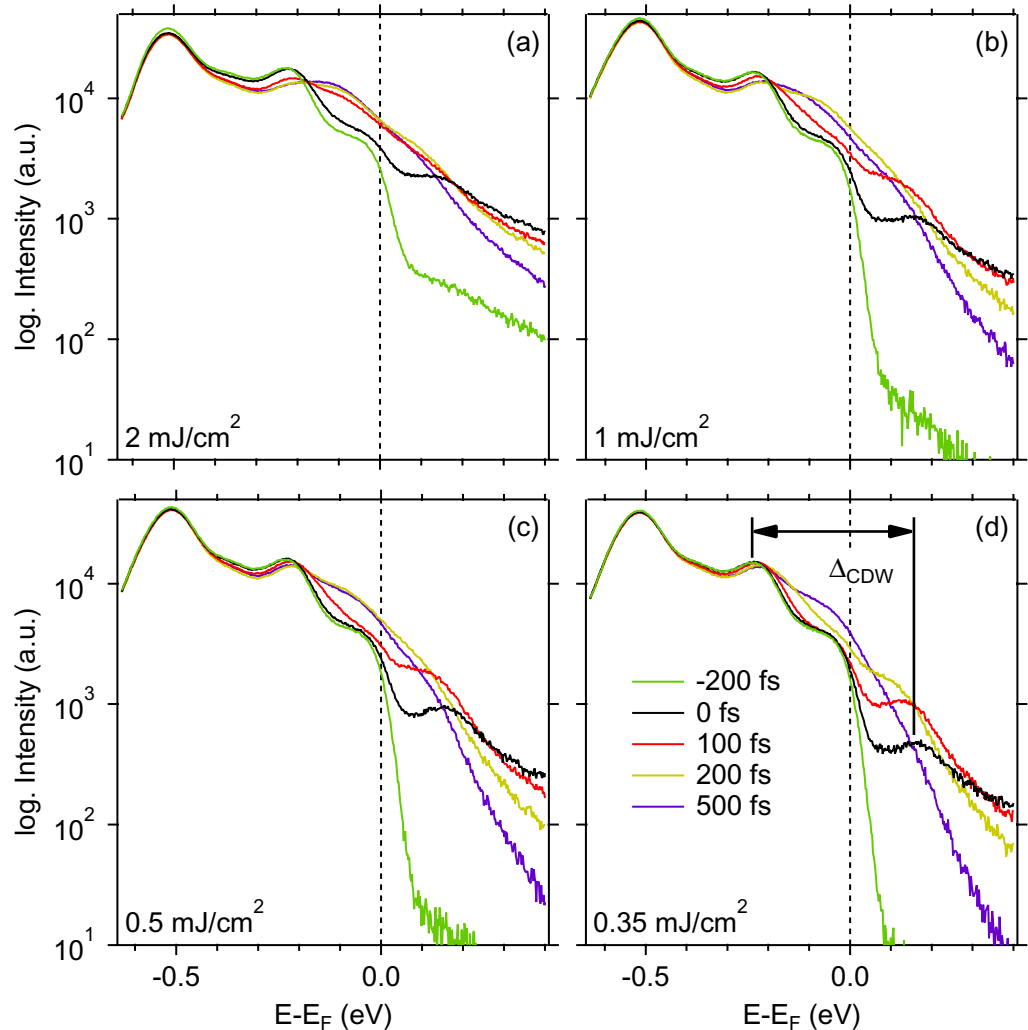
Figure 10. Half-logarithmic plot of EDCs at pump–probe delays of −200, 0, 100, 200 and 500 fs, measured at 100 K. The EDCs are taken from the data already seen in figure 8, and are presented here for fluences of $2\,\mathrm{mJ\,cm^{-2}}$ (a) down to $0.35\,\mathrm{mJ\,cm^{-2}}$ (d). The non-zero background above E_F before pumping is due to secondary electrons emitted from the IR pump pulse. The CDW gap was determined by the energy distance of the maxima of the band's second derivative at $t = 0$ and is indicated.

Alternatively, a non-uniform, 'patch-like' melting might also be possible. Although the occupied part of the CDW band vanishes almost completely at high fluences (cf figure 10(a)), still no well-defined quasi-particle band appears at E_F at later delays. The absence of a well-defined CDW peak at later delays—even at high fluences where the charge order melts—is contrary to an adiabatic melting of the charge order, since that would give rise to a Lorentzian peak at E_F. This observation points out where the simple equilibrium analogy describing the CDW transition fails. Thus we conclude that the transient photoinduced metallic state we observe here is qualitatively different from the metallic equilibrium state above T_{CDW}.

Turning to the dynamics of the peak of the unoccupied CDW band, we note that this feature disappears faster with increasing fluence. This might be explained by the increasingly intense hot electron distribution function, which conceals the unoccupied CDW peak. Also, the excited electrons in the unoccupied CDW band thermalize much quicker because of the increased e–e scattering phase space due to the higher excitation density. Still, it is unclear whether this can explain the fast disappearance at high fluences, since even though the thermalization is quicker, the overall energy relaxation towards E_F is slower, as empty states above E_F needed for electron–hole pair creation are increasingly occupied with photoexited electrons at higher pump fluences.

4. Discussion

The qualitative differences observed in the response of the CDW band between the gapped and ungapped (cf figures 5, 7 and 9) regions in the BZ and the appearance of a new collective mode as a function of the BZ position, temperature and fluence allow us to draw further conclusions. The transient changes in the binding energies result from a combination of a dynamic electronic susceptibility and coupling of electrons with bosonic modes. The essence of our observations can be captured by invoking a simple picture of basic CDW physics [6]: it is already known that the electron–phonon coupling must be large and possibly anisotropic [47] in TbTe$_3$ in order to open CDW bandgaps of the order of several hundreds of meVs as observed by ARPES [27, 34, 48] and optical conductivity [49]. Furthermore, the unscreened electronic susceptibility $\chi(E, \vec{k})$, which contributes to a nesting-driven CDW [26, 33, 35], peaks at E_F.

Comparing the band dispersion of the low-temperature, gapped CDW state (figures 3(b) and (d)) to the high-temperature, mostly ungapped state (figures 3(g) and (i)) in thermal equilibrium, it is evident that the largest changes in the band structure occur directly at E_F in the CDW nesting region due to the closing of the CDW gap. In turn, the transient spectra also present the largest changes in the CDW band at E_F in the nesting region. This transient closing of the CDW bandgap occurs on a timescale of ∼100 fs and can be interpreted as an ultrafast transition from the gapped CDW state to an ungapped state, which resembles the metallic, ungapped high-temperature state. In general, this analogy holds since the bands retain a quasi-particle-like character even though the excitations are strong enough to induce an ultrafast closing, or 'melting' of the CDW bandgap [16].

This simple analogy to equilibrium physics can explain two of our major observations. Firstly, the response of the CDW system is strongly anisotropic and maximal at E_F in the nesting region, accounting for the pronounced momentum-dependent response and the closing of the CDW bandgap upon femtosecond laser excitation. Secondly, the emergence of a collective mode that is exclusively observed in the gapped CDW state points to the excitation of the CDW amplitude mode.

Considering that CDW formation requires FS nesting and freezing out of a particular vibration at momentum Q_{CDW}, melting requires 'reactivation' of that specific mode, i.e. ion core motion. This interpretation implies a finite timescale for the closing of the CDW bandgap, i.e. a delayed response to the laser excitation (cf figures 8 and 9(b)). Since the timescale of the closing of the bandgap is closely related to the frequency of the CDW amplitude mode of frequency f [6], one might anticipate that it takes a time of at least $\frac{1}{4f}$ to close the bandgap. Taking the first maximum of the coherent oscillations as an estimate, a continuous decrease in the peak position from ∼300 fs at low fluences to about 150 fs at high fluences is detected.

This observation is consistent with the idea that the timescale of the CDW bandgap closing is governed by the frequency of the amplitude mode, i.e. the collective oscillations in the upper CDW band. However, a detailed discussion of the correlation of the timescale of the bandgap closing and coherent oscillations will be presented in future work [50].

The fluence dependence of the frequency seen in figure 9(e) is in agreement with the photoinduced CDW melting. At excitation densities below the transition barrier, the CDW amplitude mode is discerned well ($F = 0.35\,\mathrm{mJ\,cm^{-2}}$) with 2.5(5) THz. Increasing F results in a rather complex behavior, where the initial oscillations still resemble the 2.5 THz mode, but at delays $> 1\,\mathrm{ps}$, the 3.5 THz mode is encountered ($F = 0.5\,\mathrm{mJ\,cm^{-2}}$). This suggests that it requires about 1 ps until the ungapped metal-like state is fully formed and the CDW amplitude mode is fully lost. When going to even higher fluences ($F = 1\,\mathrm{mJ\,cm^{-2}}$), a complex behavior is encountered with no single discernible frequencies. The system seems to be in a mixed state, and the crossover between weak and strong perturbations thus happens right at this fluence of $F = 1\,\mathrm{mJ\,cm^{-2}}$. At the highest fluences ($F \geqslant 2\,\mathrm{mJ\,cm^{-2}}$), a fast oscillation is visible, which softens over time. At these highest fluences, the gap seems to be fully closed (as marked by the first maximum in the center-of-mass traces in figure 9(b)) at $\approx 100\,\mathrm{fs}$.

Interestingly, not only is a strongly fluence-dependent initial response of the CDW peak observed but also the timescale for the relaxation of the photoexcited state depends on the fluence. As evident from figures 8 and 9(b), the initial binding energy shift has relaxed after $\sim 2\,\mathrm{ps}$ to about 15% of its maximum value for fluences $\leqslant 1\,\mathrm{mJ\,cm^{-2}}$. For fluences exceeding $1\,\mathrm{mJ\,cm^{-2}}$, where the strong perturbation regime is entered and the charge order melts, the binding energy shift lasts much longer and even after 2 ps remains at $\sim 90\%$ of its initial value for $3\,\mathrm{mJ\,cm^{-2}}$. One might speculate that this nonlinear relaxation behavior as a function of excitation density points to a transient change of the e–ph coupling strength. Since e–e scattering merely redistributes the optically deposited excess energy in the thermalization process amongst other electrons, the main energy dissipation channel for the excited electron system is e–ph coupling. The large CDW band gap size of 400 meV underlines a large e–ph coupling as an ingredient for the CDW formation. Under strong excitation conditions, the electronic screening of the ion cores is altered, which initiates the excitation of the CDW amplitude mode and might also affect the e–ph coupling strength, resulting in the observed threshold behavior of the energy relaxation times when the CDW melts.

Clearly, the time-dependent frequency softening of the collective mode in the CDW band for large excitation densities points to physics beyond the Born–Oppenheimer approximation [51]. The initial softening of the mode can be understood by a change in the excited potential energy surface in which the ions move. This change occurs during the first 0.8 ps, which corresponds to the timescale of the electron thermalization process. At later delays, the CDW state is molten and we observe weak oscillations originating from the strong coherent oscillations of the lower band.

Our temperature-, momentum- and fluence-dependent results allow an assignment of the 2.5 THz mode to the CDW amplitude mode. Other origins of this mode can be excluded, as we detail in the following. Calculated phonon dispersions for RTe_3 show modes at 2.3 THz [52]. However, these generic phonon modes do not exhibit the temperature-, momentum- or fluence dependence we observe here. Another possibility is a phonon mode, which is created by the symmetry breaking due to the CDW. Lavagnini *et al* observe a feature near 2.6 THz in $LaTe_3$, 2.5 THz for $SmTe_3$ [52] and 2.3 THz for $DyTe_3$ [53] via Raman scattering. This feature weakens when going from the distorted to the undistorted crystal structure. In principle, this could explain

the temperature dependence, since this mode requires the CDW symmetry breaking. However, our observation of a pronounced BZ-position dependence of the 2.5 THz mode and its exclusive presence in the CDW band make this assignment unlikely. On the other hand, a collective excitation of the CDW amplitude mode naturally explains the dependence of the excitations on the BZ position, its temperature dependence and the fact that the mode is present exclusively in the CDW band in the gapped region.

Moreover, a temperature-dependent softening of a mode at 2.3 THz in TbTe$_3$ was observed via time-resolved optical reflectivity measurements at pump fluences about 10 times smaller than the ones used in our experiments [54] and via Raman scattering [53]. Close to T_{CDW}, the mode softening follows the predictions by mean field theory [6], but is suppressed at lower temperatures, which was explained by resonant coupling to a mode at 1.75 THz [54] or as due to interactions between two perpendicular CDW modes. However, below T_{CDW}, a new mode appears at 2.3 THz. Due to its characteristic temperature-dependent softening [6], it is assigned to the CDW amplitude mode. These results are consistent with recent temperature-dependent Raman studies [53], where modes near 2.2 THz are observed in DyTe$_3$ and LaTe$_3$, respectively, which soften with increasing temperature and hence are assigned to the CDW amplitude mode.

In contrast, we observe the 3.5 THz mode independently of temperature, momentum and pump fluence and thus assign this mode to a generic coherent phonon of TbTe$_3$. However, as tr-ARPES observes phonon modes through their coupling to the electronic band structure, a knowledge of the band character and their coupling to particular modes is desirable for identification. Since the lower band eludes a theoretical description so far, the 3.5 THz mode is assigned via comparison to other experiments. Lavagnini *et al* observe a mode in DyTe$_3$ at 3.9 THz [53]. Interestingly, this mode disappears with increasing temperature above T_{CDW} but does not exhibit mode softening with increasing temperature, which would be characteristic of the CDW amplitude mode. Because the symmetry of this mode requires CDW symmetry breaking to be observable in their Raman geometry, this mode might result from the super-lattice periodicity induced by the CDW but does not constitute a collective excitation of the CDW amplitude mode itself.

5. Conclusion and outlook

We have presented a temperature-, momentum- and fluence-dependent tr-ARPES study of the ultrafast electron dynamics in the nesting-driven CDW compound TbTe$_3$. Our main results are as follows. (i) The identification of a coherent mode at 3.5 THz, which does not depend on the BZ position, the temperature or the excitation density. Thus, it is assigned to a generic coherent phonon of TbTe$_3$. (ii) In contrast, we observe a coherent mode at 2.5 THz only for $T \ll T_{CDW}$, in the CDW nesting region and at low fluences, where the CDW state is not quenched. Its close relation to the CDW state characterizes this mode as the collective excitation of the CDW amplitude mode. Furthermore, we investigated the fluence-dependent crossover between an ultrafast melting of the CDW phase at high excitation densities and a gentle perturbation, resulting in the coherent excitation of the CDW amplitude mode.

Future investigations will consider (i) the detailed temperature dependence of the collective mode in the CDW band to facilitate a comparison with mean-field theory; (ii) how the excited electrons dissipate the excess energy to collective modes, i.e. which scattering channels are favored due to phase space and symmetry arguments; (iii) where in the BZ optical transitions and thus the creation of e–h pairs are allowed; and (iv) how the e–ph coupling changes as a function

IOP Institute of Physics **Φ** DEUTSCHE PHYSIKALISCHE GESELLSCHAFT

of energy and momentum [47]. Further interesting questions might be answered by our data when compared to a more quantitative theory, such as dynamical mean-field theory employing the two-time formalism of the Falicov–Kimball model [55–58]: (i) what is the microscopic picture for the CDW melting, i.e. does it melt in 'patches' and to what degree are the fluctuations that are excited by the laser excitation homogeneous or inhomogeneous (which has recently been addressed by Yusupov *et al*? [59]); (ii) to what extent do surface termination effects play a role?; (iii) could the CDW melting be induced by dissipation of the strong 3.5 THz phonon to the lower band?

Acknowledgments

References

[1] Sachdev S 2001 *Quantum Phase Transitions* (Cambridge: Cambridge University Press)
[2] Mahan G D 1990 *Many-Particle Physics* 2nd edn (New York and London: Plenum)
[3] Fetter A L and Walecka J D 2003 *Quantum Theory of Many-Particle Systems* (Mineola, NY: Dover)
[4] Fulde P, Schmidt B and Thalmeier P 1995 Theoretical model for the semi-metal Yb_4As_3 *Europhys. Lett.* **31** 323
[5] Damascelli A, Hussain Z and Shen Z-X 2003 Angle-resolved photoemission studies of the cuprate superconductors *Rev. Mod. Phys.* **75** 473
[6] Grüner G 1994 Density waves in solids (*Frontiers in Physics* vol 89) (Reading, MA: Addison-Wesley)
[7] Fulde P, Thalmeier P and Zwicknagl G 2006 Strongly correlated electrons (*Solid State Physics* vol 60) (New York: Academic Press) pp 1–180
[8] Löhneysen H v, Rosch A, Vojta M and Wölfle P 2007 Fermi-liquid instabilities at magnetic quantum phase transitions *Rev. Mod. Phys.* **79** 1015–75
[9] Pfleiderer C 2009 Superconducting phases of f-electron compounds *Rev. Mod. Phys.* **81** 1551–624
[10] Tinkham M 2004 *Introduction to Superconductivity* (Mineola, NY: Dover)
[11] Bardeen J, Cooper L N and Schrieffer J R 1957 Theory of superconductivity *Phys. Rev.* **106** 162
[12] Hüfner S 1995 *Photoelectron Spectroscopy* (Berlin: Springer)
[13] Hofmann A *et al* 2009 Renormalization of bulk magnetic electron states at high binding energies *Phys. Rev. Lett.* **102** 187204
[14] Perfetti L, Loukakos P A, Lisowski M, Bovensiepen U, Eisaki H and Wolf M 2007 Ultrafast electron relaxation in superconducting $Bi_2Sr_2CaCu_2O_{8+\delta}$ by time-resolved photoelectron spectroscopy *Phys. Rev. Lett.* **99** 197001
[15] Bovensiepen U 2007 Coherent and incoherent excitations of the Gd(0001) surface on ultrafast timescales *J. Phys.: Condens. Matter* **19** 083201
[16] Schmitt F *et al* 2008 Transient electronic structure and melting of a charge density wave in $TbTe_3$ *Science* **321** 1649
[17] Matsumoto Y and Watanabe K 2006 Coherent vibrations of adsorbates induced by femtosecond laser excitation *Chem. Rev.* **106** 4234–60

[18] Chulkov E V, Borisov A G, Gauyacq J P, Sanchez-Portal D, Silkin V M, Zhukov V P and Echenique P M 2006 Lifetimes of image-potential states on copper surfaces *Chem. Rev.* **106** 4160

[19] Rhie H-S, Dürr H A and Eberhardt W 2003 Femtosecond electron and spin dynamics in Ni/W(110) films *Phys. Rev. Lett.* **90** 247201

[20] Lisowski M, Loukakos P A, Melnikov A, Radu I, Ungureanu L, Wolf M and Bovensiepen U 2005 Femtosecond electron and spin dynamics in Gd(0001) studied by time-resolved photoemission and magneto-optics *Phys. Rev. Lett.* **95** 137402

[21] Miaja-Avila L, Lei C, Aeschlimann M, Gland J L, Murnane M M, Kapteyn H C and Saathoff G 2006 Laser-assisted photoelectric effect from surfaces *Phys. Rev. Lett.* **97** 113604

[22] Cavalieri A L *et al* 2007 Attosecond spectroscopy in condensed matter *Nature* **449** 1029

[23] Loukakos P A, Lisowski M, Bihlmayer G, Blügel S, Wolf M and Bovensiepen U 2007 Dynamics of the self-energy of the Gd(0001) surface state probed by femtosecond photoemission spectroscopy *Phys. Rev. Lett.* **98** 097401

[24] Perfetti L, Loukakos P A, Lisowski M, Bovensiepen U, Berger H, Biermann S, Cornaglia P S, Georges A and Wolf M 2006 Time evolution of the electronic structure of $1T\text{-}TaS_2$ through the insulator–metal transition *Phys. Rev. Lett.* **97** 067402

[25] Ru N and Fisher I R 2006 Thermodynamic and transport properties of YTe_3, $LaTe_3$, and $CeTe_3$ *Phys. Rev.* B **73** 033101

[26] Ru N, Condron C L, Margulis G Y, Shin K Y, Laverock J, Dugdale S B, Toney M F and Fisher I R 2008 Effect of chemical pressure on the charge density wave transition in rare-earth tritellurides RTe_3 *Phys. Rev.* B **77** 035114

[27] Brouet V *et al* 2008 Arpes study of the evolution of band structure and charge density wave properties in RTe_3 for R = Y, La, Ce, Sm, Gd, Tb and Dy *Phys. Rev.* B **77** 235104

[28] Malliakas C D, Billinge S J L, Kim H J and Kanatzidis M G 2005 Square nets of Tellurium: Rare-earth dependent variation in the charge-density wave of $RETe_3$ (RE = rare-earth element) *J. Am. Chem. Soc.* **127** 6510

[29] Malliakas C D and Kanatzidis M G 2006 Divergence in the behavior of the charge density wave in $RETe_3$ (RE = rare-earth element) with temperature and RE element *J. Am. Chem. Soc.* **128** 12612

[30] DiMasi E, Aronson M C, Mansfield J F, Foran B and Lee S 1995 Chemical pressure and charge density waves in rare-earth tritellurides *Phys. Rev.* B **52** 14516

[31] Laverock J, Dugdale S B, Major Zs, Alam M A, Ru N, Fisher I R, Santi G and Bruno E 2005 Fermi surface nesting and charge-density wave formation in rare-earth tritellurides *Phys. Rev.* B **71** 085114

[32] Brouet V, Yang W L, Zhou X J, Hussain Z, Ru N, Shin K Y, Fisher I R and Shen Z X 2004 Fermi surface reconstruction in the CDW state of $CeTe_3$ observed by photoemission *Phys. Rev. Lett.* **93** 126405

[33] Moore R G, Brouet V, He R, Lu D H, Ru N, Chu J-H, Fisher I R and Shen Z-X 2010 Fermi surface evolution across multiple charge density wave transitions in $ErTe_3$ *Phys. Rev.* B **81** 073102

[34] Gweon G-H, Denlinger J D, Clack J A, Allen J W, Olson C G, DiMasi E, Aronson M C, Foran B and Lee S 1998 Direct observation of complete Fermi surface, imperfect nesting, and gap anisotropy in the high-temperature incommensurate charge-density-wave compound $SmTe_3$ *Phys. Rev. Lett.* **81** 886

[35] Fang A, Ru N, Fisher I R and Kapitulnik A 2007 STM studies of $TbTe_3$: evidence for a fully incommensurate charge density wave *Phys. Rev. Lett.* **99** 046401

[36] Kim H J, Malliakas C D, Tomi A T, Tessmer S H, Kanatzidis M G and Billinge S J L 2006 Local atomic structure and discommensurations in the charge density wave of $CeTe_3$ *Phys. Rev. Lett.* **96** 226401

[37] Lisowski M, Loukakos P A, Bovensiepen U, Stähler J, Gahl C and Wolf M 2004 Ultra-fast dynamics of electron thermalization, cooling and transport effects in Ru(001) *Appl. Phys.* A **78** 165

[38] Perfetti L, Loukakos P A, Lisowski M, Bovensiepen U, Wolf M, Berger H, Biermann S and Georges A 2008 Femtosecond dynamics of electronic states in the Mott insulator $1T\text{-}TaS_2$ by time-resolved photoelectron spectroscopy *New J. Phys.* **10** 053019

IOP Institute of Physics **ⅅ** DEUTSCHE PHYSIKALISCHE GESELLSCHAFT

[39] Rethfeld B, Kaiser A, Vicanek M and Simon G 2002 Ultrafast dynamics of nonequilibrium electrons in metals under femtosecond laser irradiation *Phys. Rev.* B **65** 214303

[40] Anisimov S I, Kapeliovich B L and Perelman T L 1974 Electron emission from metal surfaces exposed to ultrashort laser pulses *Sov. Phys.—JETP* **39** 375

[41] Dekorsy T, Cho G and Kurz H 2000 Coherent phonons in condensed media *Light Scattering in Solids VIII* ed M Cardona and G Güntherodt (*Topics in Applied Physics* vol 76) (Berlin: Springer) pp 169–209

[42] Ishioka K and Misochko O V 2010 Coherent lattice oscillations in solids and their optical control (*Progress in Ultrafast Intense Laser Science* vol 5) (Berlin: Springer) pp 23–63

[43] Zeiger H J, Vidal J, Cheng T K, Ippen E P, Dresselhaus G and Dresselhaus M S 1992 Theory for displacive excitation of coherent phonons *Phys. Rev.* B **45** 768–78

[44] Petek H and Ogawa S 1997 Femtosecond time-resolved two-photon photoemission studies of electron dynamics in metals *Prog. Surf. Sci.* **56** 239

[45] Lee P A, Citrin P H, Eisenberger P and Kincaid B M 1981 Extended x-ray absorption fine structure—its strengths and limitations as a structural tool *Rev. Mod. Phys.* **53** 769–806

[46] Echenique P-M, Berndt R, Chulkov E-V, Fauster Th, Goldmann A and Höfer U 2004 Decay of electronic excitations at metal surfaces *Surf. Sci. Rep.* **52** 219

[47] Johannes M D and Mazin I I 2008 Fermi surface nesting and the origin of charge density waves in metals *Phys. Rev.* B **77** 165135

[48] Sacchetti A *et al* 2009 Pressure-induced quenching of the charge-density-wave state in rare-earth tritellurides observed by X-ray diffraction *Phys. Rev.* B **79** 201101

[49] Sacchetti A, Arcangelett E, Perucchi A, Baldassarre L, Postorino P, Lupi S, Ru N, Fisher I R and Degiorgi L 2007 Pressure dependence of the charge-density-wave gap in rare-earth tritellurides *Phys. Rev. Lett.* **98** 026401

[50] Kirchmann P S, Schmitt F T and Bovensiepen U in preparation

[51] Ishioka K, Hase M, Kitajima M, Wirtz L, Rubio A and Petek H 2008 Ultrafast electron–phonon decoupling in graphite *Phys. Rev.* B **77** 121402

[52] Lavagnini M *et al* 2008 Evidence for coupling between charge density waves and phonons in two-dimensional rare-earth tritellurides *Phys. Rev.* B **78** 201101

[53] Lavagnini M, Eiter H-M, Tassini L, Muschler B, Hackl R, Monnier R, Chu J-H, Fisher I R and Degiorgi L 2010 Raman scattering evidence for a cascade evolution of the charge-density-wave collective amplitude mode *Phys. Rev.* B **81** 081101

[54] Yusupov R V, Mertelj T, Chu J-H, Fisher I R and Mihailovic D 2008 Single-particle and collective mode couplings associated with 1- and 2-directional electronic ordering in metallic RTe$_3$ (R = Ho, Dy, Tb) *Phys. Rev. Lett.* **101** 246402

[55] Freericks J K and Zlatić V 2003 Exact dynamical mean-field theory of the Falicov–Kimball model *Rev. Mod. Phys.* **75** 1333

[56] Freericks J K, Turkowski V M and Zlatić V 2006 Nonequilibrium dynamical mean-field theory *Phys. Rev. Lett.* **97** 266408

[57] Freericks J K 2008 Quenching Bloch oscillations in a strongly correlated material: nonequilibrium dynamical mean-field theory *Phys. Rev.* B **77** 075109

[58] Moritz B, Devereaux T P and Freericks J K 2010 Time-resolved photoemission of correlated electrons driven out of equilibrium *Phys. Rev.* B **81** 165112

[59] Yusupov R, Mertelj T, Kabanov V V, Brazovskii S, Kusar P, Chu J-H, Fisher I R and Mihailovic D 2010 Coherent dynamics of macroscopic electronic order through a symmetry breaking transition *Nat. Phys.* **6** 681–4